Competing topological superconducting phases in $FeSe_{0.45}Te_{0.55}$

Chang Xu, Ka Ho Wong, Eric Mascot, and Dirk K. Morr
Department of Physics, University of Illinois at Chicago, Chicago, Illinois 60607, USA

(Received 23 November 2022; revised 11 May 2023; accepted 15 May 2023; published 15 June 2023)

We demonstrate that recent angle-resolved photoemission spectroscopy experiments provide strong evidence for the existence of two competing topological superconducting phases in $FeSe_{0.45}Te_{0.55}$. The coupling of their underlying microscopic mechanisms—one based on a three-dimensional topological insulator, one based on two-dimensional superconductivity—stabilizes topological superconductivity over a wide range of parameters, and gives rise to two disjoint topological regions in the phase diagram of $FeSe_{0.45}Te_{0.55}$. We show that the topological origin of these regions can be identified by considering the form of Majorana edge modes at domain walls.

DOI: 10.1103/PhysRevB.107.214514

I. INTRODUCTION

Topological superconductors harbor Majorana zero modes, whose non-Abelian braiding statistics and robustness against disorder and decoherence provide a new platform for the implementation of topological quantum computing [1]. Over the past few years, strong evidence for the existence of topological surface superconductivity in the iron-based superconductor $FeSe_{0.45}Te_{0.55}$ has emerged, ranging from the observation of a surface Dirac cone [2–5] to that of Majorana zero modes (MZMs) in vortex cores [6–9] and of Majorana edge modes at domain walls [10]. However, the microscopic origin of these topological features has remained unclear. Although they were originally attributed [2,11–13] to topological surface superconductivity arising from a Fu-Kane-like mechanism [14] of proximity-induced superconductivity in the surface Dirac cone of a three-dimensional topological insulator—referred to as the 3DTI mechanism—, recent experiments have cast doubt on this interpretation. In particular, angle-resolved photoemission spectroscopy (ARPES) experiments [3–5] on $FeSe_{1-x}Te_x$ and quantum sensing experiments on $FeSe_{0.3}Te_{0.7}$ [15], reported evidence for surface ferromagnetism [4], which can readily destroy the 3DTI mechanism [16]. An alternative scenario [17,18]—the two-dimensional topological superconductivity (2DTSC) mechanism—was, therefore, proposed in which the 2D nature of superconductivity in the α, β and γ bands of $FeSe_{0.45}Te_{0.55}$ [19–23], in combination with the observed surface magnetism [3–5,15] induces topological superconductivity. Interestingly enough, the experimentally observed opening of a gap at E_F in the Dirac cone at T_c [4]—reflecting proximity induced superconductivity—implies a coupling of these two competing mechanisms. The question, thus, naturally arises of how the interplay between the competing 2DTSC and 3DTI mechanisms determines the topological properties and phase diagram of $FeSe_{0.45}Te_{0.55}$.

In this article, we address this question and demonstrate that the competition between these two mechanisms can not only explain the experimentally observed opening of two gaps in the surface Dirac cone of $FeSe_{0.45}Te_{0.55}$ —at E_F and at the Dirac point [4]—but also gives rise to two disjoint topological regions in the phase diagram: a small magnetic moment region in which topological superconductivity arises from the 3DTI mechanism, and a large magnetic moment region whose topological properties are determined by the 2DTSC mechanism. We demonstrate that the topological nature of these regions can be unambiguously identified by considering the electronic structure and currents near spin and π-phase domain walls. Our results provide unique characteristics allowing future experiments to elucidate the microscopic origin of the topological superconducting phases of $FeSe_{0.45}Te_{0.55}$.

II. THEORETICAL FORMALISM

To study the emergence of topological surface superconductivity in $FeSe_{0.45}Te_{0.55}$, we consider a 3D system with N_z layers [see Fig. 1(a)]. The originally proposed 2DTSC mechanism [17] utilizes a five-orbital model [24], arising from the five Fe d orbitals, that has been previously employed to successfully describe the two-dimensional superconducting properties of the iron-based superconductors [23]. However, to meet the computational demands of the present study we are required to utilize a simplified version of this 2DTSC model [17], which nevertheless preserves its salient features (see Appendix A). In particular, the simplified version still reproduces the experimentally observed [25] two Fermi surfaces that are closed around the Γ point, which are relevant for the coupling to the Dirac cone. Moreover, the quasi-2D nature of superconductivity in $FeSe_{1-x}Te_x$ as observed by ARPES experiments [20–23] implies zero direct coupling between the 2DTSC layers, yielding the Hamiltonian,

$$\begin{aligned} H_{2DTSC} = &-t\sum_{\langle \mathbf{r}\mathbf{r}'\rangle,\sigma,n} f^{\dagger}_{n,\mathbf{r},\sigma} f_{n,\mathbf{r}',\sigma} - \mu \sum_{\mathbf{r},\sigma} f^{\dagger}_{n,\mathbf{r},\sigma} f_{n,\mathbf{r},\sigma} \\ &+ \Delta_0 \sum_{n,\mathbf{r}} f^{\dagger}_{n,\mathbf{r},\uparrow} f^{\dagger}_{n,\mathbf{r},\downarrow} + \text{H.c.} \\ &+ \sum_{n=1,N_z} g_n \Bigg(i\alpha \sum_{\mathbf{r},\boldsymbol{\delta},\sigma,\sigma'} f^{\dagger}_{n,\mathbf{r},\sigma} [\boldsymbol{\delta}\times\boldsymbol{\sigma}]^z_{\sigma,\sigma'} f_{n,\mathbf{r}+\boldsymbol{\delta},\sigma'} \\ &- JS \sum_{\mathbf{r},\sigma,\sigma'} f^{\dagger}_{n,\mathbf{r},\sigma} \sigma^z_{\sigma\sigma'} f_{n,\mathbf{r},\sigma'} \Bigg), \end{aligned} \tag{1}$$

 ©2023 American Physical Society

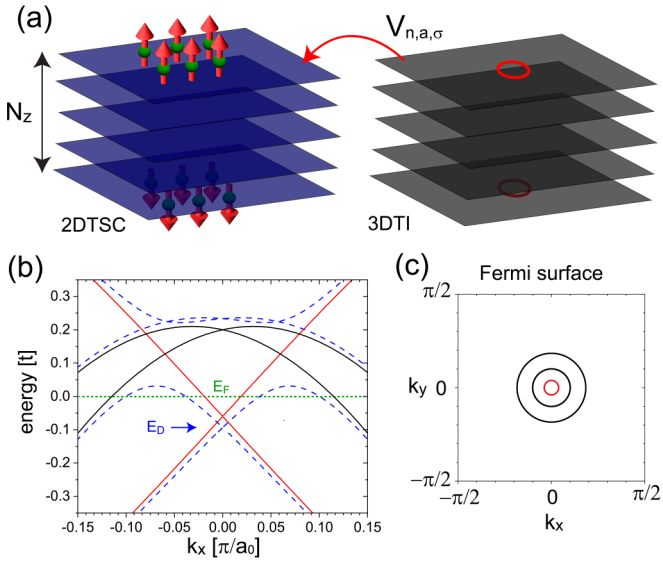

FIG. 1. (a) Schematic representation of the coupled 3DTI and 2DTSC systems with N_z layers. (b) Surface electronic structure: solid red and black lines represent the decoupled 3DTI and 2DTSC ($V = 0$) systems, respectively, dashed lines the coupled ones ($V \neq 0$). (c) Fermi surface of the coupled system. Parameters are $(JS, \alpha, \mu, \mu_c) = (0, 0.1, 3.8, 0.06)t$.

where $f^\dagger_{n,\mathbf{r},\sigma}$ creates an electron with spin σ at site $\mathbf{r}$ in layer $n = 1, \ldots, N_z$, $-t$ is the electronic hopping amplitude between nearest-neighbor sites on a 2D square lattice, μ is the chemical potential, Δ_0 is the s-wave superconducting order parameter, α is the Rashba spin-orbit coupling, J is the magnetic exchange coupling, and S is the ordered moment. We take the experimentally observed out-of-plane magnetism and Rashba spin-orbit interaction arising from a broken inversion symmetry to be present on the top and bottom surfaces only with $g_1 = -g_{N_z} = 1$ as required by symmetry (see Appendix A).

In contrast, the 3DTI mechanism is based on the observation that the hybridization of the d_{xy} and p_z orbitals along the z axis in $FeSe_{0.45}Te_{0.55}$ leads to a band inversion and the emergence of a 3D topological insulator. Computational demands require that we simplify the actual 3DTI electronic structure of $FeSe_{0.45}Te_{0.55}$ by utilizing the following four-band Hamiltonian that was previously employed [26] to describe three-dimensional topological insulators,

$$H_{3DTI} = \sum_{\mathbf{r},j=1,2,3} \left(\Psi^\dagger_{\mathbf{r}+\hat{e}_j} \frac{-t\Gamma^1 - i\lambda\Gamma^{j+1}}{2} \Psi_{\mathbf{r}} + \text{H.c.} \right) + \sum_{\mathbf{r}} \Psi^\dagger_{\mathbf{r}} (\mu_c \Gamma^0 + m\Gamma^1) \Psi_{\mathbf{r}}, \tag{2}$$

with spinor $\Psi^\dagger_{\mathbf{r}} = (c^\dagger_{\mathbf{r},1,\uparrow}, c^\dagger_{\mathbf{r},2,\uparrow}, c^\dagger_{\mathbf{r},1,\downarrow}, c^\dagger_{\mathbf{r},2,\downarrow})$ where $c_{\mathbf{r},a,\sigma}$ annihilates an electron with spin σ in orbital $a = 1, 2$ at site $\mathbf{r}$, $\Gamma^{0,\ldots,4} = (\mathbb{1} \otimes \mathbb{1}, \mathbb{1} \otimes s_z, -\sigma_y \otimes s_x, \sigma_x \otimes s_x, -\mathbb{1} \otimes s_y)$ with σ_i and s_i $(i = x, y, z)$ being Pauli matrices, μ_c is the chemical potential, and λ is the spin-orbit coupling. We take $m = 2t$ and, for simplicity, choose $\lambda = t$ such that the system is in the topological phase [26] and consider a 3DTI with N_z layers. The coupling between the 3DTI and the 2DTSC layers is described by the Hamiltonian,

$$H_{\text{hyb}} = -\sum_{n,\mathbf{r},a,\sigma} V_{n,a,\sigma} f^\dagger_{n,\mathbf{r},\sigma} c_{n,\mathbf{r},a,\sigma} + \text{H.c.}, \tag{3}$$

with $V_{n,a,\sigma}$ being the hybridization strength in the n'th layer. The relative signs of $V_{n,a,\sigma}$ are determined by the rotation symmetry of the coupled system (see Appendix B).

III. RESULTS

In Fig. 1(b), we present the electronic dispersion of the decoupled ($V = 0$) and coupled ($V \neq 0$) 3DTI and the 2DTSC systems above T_c where $JS = 0$. The dispersion exhibits a Dirac cone with a Dirac point located at E_D and two hole-like bands of the 2DTSC, which are split by the Rashba spin-orbit interaction [25]. For $V \neq 0$, the 3DTI and 2DTSC bands hybridize, thus, opening a hybridization gap at the band crossings. The resulting Fermi surfaces shown in Fig. 1(c), with the innermost (red) one arising predominantly from the Dirac cone, and the two outer (black) ones due to the 2DTSC bands, are in qualitative agreements with the experimental ARPES observations [2]. To describe the experimentally observed temperature evolution of the spectral function below T_c [4], and specifically, the opening of gaps at the Fermi energy and at the Dirac point, we assume an onset of the magnetic order ($JS \neq 0$) at T_c with JS increasing with decreasing temperature. The resulting evolution of the electronic structure and (3DTI) c-electron surface spectral functions is shown in Fig. 2 (the f-electron spectral function is shown in Appendix C). Just below T_c, [see Fig. 2(a)], the hybridization between the 2DTSC and the 3DTI system proximity induces a superconducting gap Δ_{SC} in the 3DTI Dirac cone at E_F. At the same time, a nonzero magnetization $JS \neq 0$ leads to a magnetic polarization in the Dirac cone, opening a gap Δ_D at the Dirac point. As we demonstrate below, this renders the system a Fu-Kane-type topological superconductor [14]. With increasing JS, both Δ_{SC} and Δ_D further increase [see Fig. 2(b)], in good qualitative agreement with the temperature dependence of the spectral function observed in ARPES experiments [3–5] (see, e.g., Fig. 4 in Ref. [4]). Eventually, Δ_{SC} closes at the Γ point [see Fig. 2(c)] at $(JS)_{pt}$, which is a general feature of the coupled system and part of a line of gap closings occurring only at the Γ point (see Appendix D), resulting in two disjoint regions in the (V, JS) plane [see Fig. 2(d)]. This naturally raises the question of whether this gap closing represents a topological phase transition, and if so, what the topological nature of the involved phases in regions I and II are. To answer this question, we first note that the gap closing occurs only in the surface spectral function, whereas the bulk remains gapped, implying that it is associated with a transition affecting the topological nature of the surface phase. Moreover, we can consider two limiting cases: at $JS = 0$ and $V \neq 0$, the proximity-induced superconducting gap in the 3DTI Dirac cone is expected to lead to Fu-Kane-type [14] topological surface superconductivity, which should, thus, hold for the entire region I. In contrast, for $V \to 0$, the gap closing line terminates at a value of $(JS)_{pt}$ such that, for $JS > (JS)_{pt}$, the system is topological whereas for $JS < (JS)_{pt}$, it is trivial. Note that for $V = 0$ and $JS > (JS)_{pt}$, the 2DTSC is in the topological $C = -1$ phase. This is the same

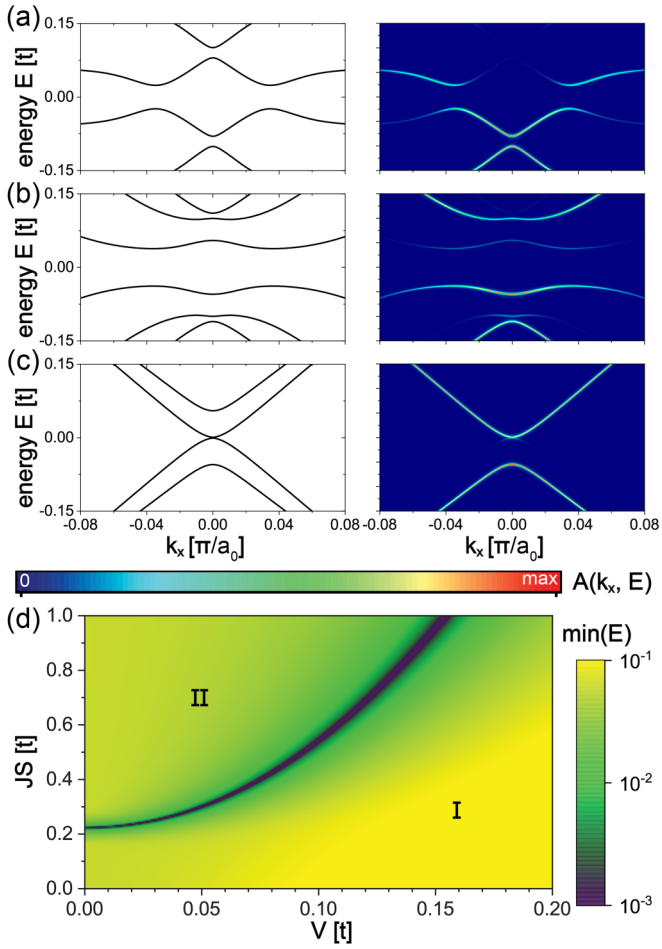

FIG. 2. Evolution of the electronic structure (left column) and spectral functions (right column, for $k_y = 0$) below T_c with increasing JS: (a) $(JS, \mu_c) = (0.1, 0.06)t$, (b) $(JS, \mu_c) = (0.2, 0.04)t$, and (c) $(JS, \mu_c) = (0.45, 0.04)t$. (d) Gap at the Γ point as a function of V and JS. Parameters are $(V, \Delta_0, \alpha, \mu) = (0.07, 0.1, 0.1, 3.8)t$ and $N_z = 5$.

topological phase obtained using a five-band model with an $s_\pm$-wave superconducting order parameter [17] (see also the discussion in Ref. [27]), thus, justifying the simplified model of Eq. (1). We, thus, conclude that in region II, the system exhibits topological surface superconductivity arising from the 2DTSC mechanism, and that the gap closing line, thus, indeed represents a topological phase transition. However, as the spectral weight in the negative energy branch of the band in which the gap closing occurs is vanishingly small [see Fig. 2(c)], the gap closings might be difficult to detect in ARPES experiments [28]. To further elucidate the topological nature of regions I and II, we next consider their electronic structure near vortices and domain walls.

IV. MZMS IN A VORTEX CORE

To explore the emergence of Majorana zero modes in magnetic vortices, we consider a system with a finite extent in the x, y, and z direction, and model a vortex [16] by assigning a phase to the local superconducting order parameter, $\Delta(\mathbf{r}) = |\Delta_0| e^{i\phi(\mathbf{r})}$, where $\phi(\mathbf{r})$ is a position-dependent angle

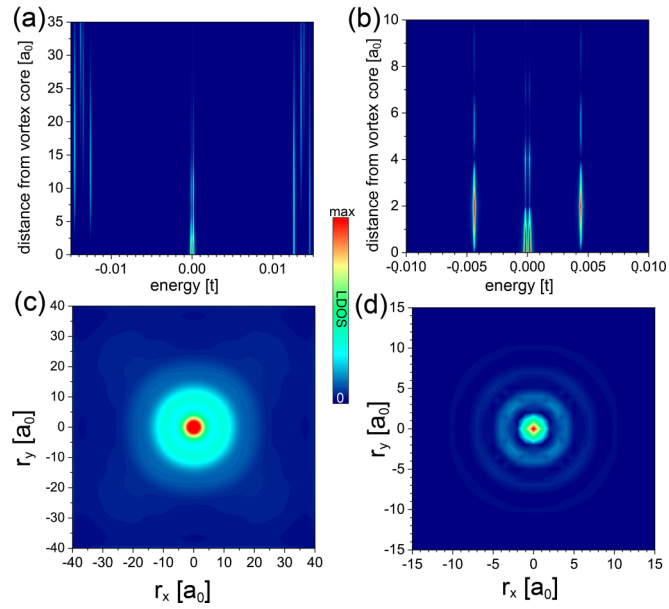

FIG. 3. Local density of state (LDOS) as a function of energy and distance from the vortex core on the top surface for (a) the c electrons in region I, and (b) the f electrons in region II (for details, see Appendix F). (c) and (d) Spatial plot of the zero-energy LDOS corresponding to (a) and (b), respectively.

(for details see Appendices E and F). In Figs. 3(a) and 3(b), we present the zero-energy LDOS along a line-cut through the vortex core in regions I and II of the phase diagram, respectively. In both cases, the LDOS exhibits a low-energy state at $E = \pm\varepsilon$, whose spatial structure at $+\varepsilon$ is shown in Figs. 3(c) and 3(d), respectively. The localization of the LDOS at the site of the vortex core, together with $\varepsilon \to 0$ with increasing system size (see also the discussion in Ref. [29]), implies that this (near) zero-energy state is an MZM and that in both regions, the superconducting surface phase is topological in nature. However, the existence of MZMs in both regions also implies that their experimental observation cannot discriminate between these two regions; this, however, can be achieved by considering the electronic structure near domains walls.

V. MAJORANA EDGE MODES ALONG DOMAIN WALLS

The emergence of Majorana edge modes at certain types of domain walls was shown to provide insight into the microscopic origin underlying topological superconductivity [17]. In particular, in a 2DTSC, a chiral Majorana edge mode emerges at a spin domain wall (SDW), where the magnetization flips its orientation $\mathbf{S} \to -\mathbf{S}$, but not a π-phase domain wall (PPDW) where the superconducting order parameter undergoes a sign change, $\Delta_0 \to -\Delta_0$ [17]. In contrast, in a Fu-Kane-type topological superconductor, a Majorana edge mode emerges at a PPDW only [14]. To test whether this qualitative difference allows us to identify the topological nature of regions I and II, we present in Figs. 4(a)–4(d) the electronic dispersion along a domain wall for a PPDW and SDW for representative parameter sets in both regions. In region I, only the PPDW exhibits an in-gap mode that traverses the superconducting gap [Fig. 4(a)], which together

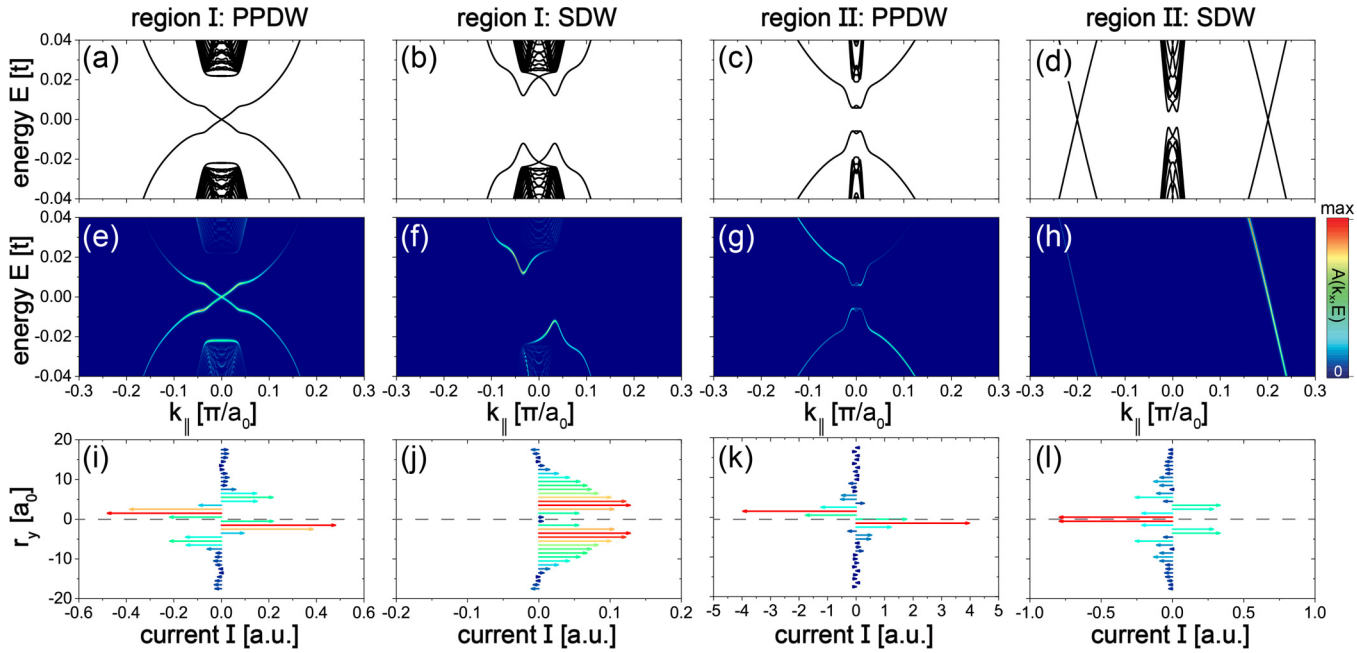

FIG. 4. (a)–(d) Electronic dispersion as a function of momentum, $k_{\parallel}$ along a PPDW and SDW domain wall for parameter sets characteristic of regions I and II (see Appendix G). Corresponding spectral functions of the (e) and (f) c electrons, and (g) and (h) f electrons. (i)–(l) Currents along the domain walls (denoted by a dashed gray line).

with its robustness against disorder effects (see Appendix G), identifies it as a Majorana edge mode. In contrast, the SDW only possesses trivial in-gap states [Fig. 4(b)], implying that topological surface superconductivity in region I arises from the Fu-Kane-like 3DTI mechanism [14]. Conversely, in region II, only a SDW exhibits a Majorana edge mode [Fig. 4(d)], which is unaffected by disorder (see Appendix G), whereas the PPDW does not [Fig. 4(c)]. Thus, in region II, topological superconductivity arises from the 2DTSC mechanism. Moreover, the complementary emergence of Majorana edge modes along a PPDW and SDW in regions I and II also implies that the topological phases arising from these two mechanisms are mutually exclusive and, thus, competing, rather than coexisting. Moreover, a plot of the spectral functions at the domain walls [see Figs. 4(e)–4(h)] reveals that the Majorana mode along the SDW in region II is chiral in nature [cf. Figs. 4(d) and 4(h)] (see Appendix G), whereas that of the PPDW in region I is neither helical nor chiral. This qualitative difference can be detected using quasiparticle interference spectroscopy [30] as the parallel Majorana branches in Fig. 4(h) lead to a nearly dispersionless peak in the quasiparticle interference spectrum [31].

The observation of a Majorana edge mode along a domain wall is, in general, not sufficient to identify the underlying microscopic origin, unless the nature of the domain wall is known. The latter can be achieved by considering the screening currents in the vicinity of domain walls (see Appendix H) as shown in Figs. 4(i)–4(l). Although both the PPDW and the SDW induce screening currents, the resulting current pattern is qualitatively different. Since the Chern number, and, hence, the chirality, is reversed at a SDW, the currents on both sides of the domain wall are symmetric, leading to a nonzero net current along the domain wall. In contrast, the current patterns on both sides of a PPDW are antisymmetric, and the net current is, thus, zero. Since the net current along a domain wall can be measured using a superconducting quantum interference device [32], its presence or absence is a crucial feature distinguishing a SDW from a PPDW. Thus, the presence or absence of a Majorana edge mode together with that of a net current allows one to unambiguously identify the nature of the domain wall and, thus, the origin of the underlying topological phase.

VI. CONCLUSIONS

We demonstrated that the opening of two gaps in the surface Dirac cone of $FeSe_{0.45}Te_{0.55}$ as reported by recent ARPES experiments [4], provides strong evidence for the existence of two competing mechanisms underlying the emergence of topological superconductivity. The competition between these mechanisms—the 2DTSC and 3DTI mechanisms—while giving rise to robust topological surface superconductivity over a large range of parameters, also produces two disjoint topological regions in parameter space. By considering the emergence of Majorana edge modes at a SDW and a PPDW, we showed that topological superconductivity in region I arises from the 3DTI mechanism, whereas that in region II is due to the 2DTSC mechanism. An important outstanding question remains: which mechanism is responsible for the topological features of $FeSe_{0.45}Te_{0.55}$, such as vortex core MZMs [7], experimentally observed at millikelvin temperatures? Although the experimental ARPES observations [4] together with our results in Fig. 2 suggest that topological superconductivity just below T_c arises from the 3DTI mechanism, they also show that with decreasing temperature, the system approaches, and potentially even crosses the

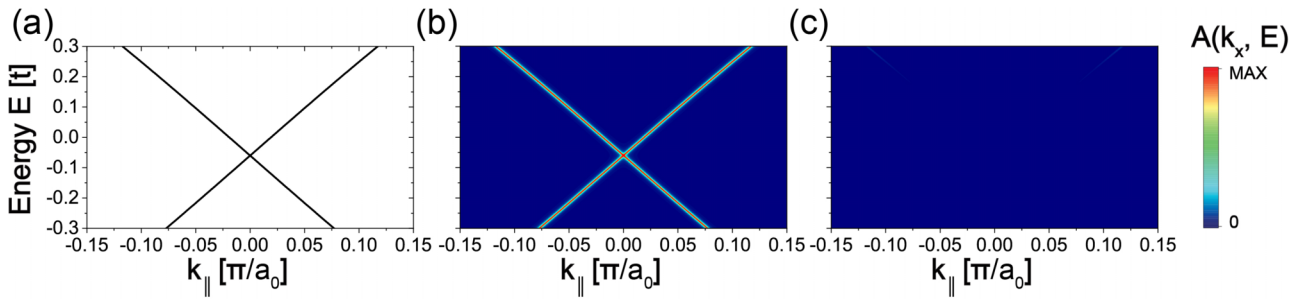

FIG. 5. (a) Surface electronic dispersion of the 3DTI ($\mu_c = 0.06t$) in normal state, revealing a Dirac cone. Spectral function of the (3DTI) c electrons (b) on the surface layer and (c) on the first layer below the surface.

topological phase transition into region II; a transition which might be difficult to observe via ARPES due to the vanishingly small spectral weight in the gap closing bands. Clearly, future experiments are required to elucidate the nature of the topological phase in $FeSe_{0.45}Te_{0.55}$ at the lowest temperatures.

ACKNOWLEDGMENTS

We thank P. Johnson and S. Rachel for stimulating discussions. This work was supported by the U. S. Department of Energy, Office of Science, Basic Energy Sciences, under Award No. DE-FG02-05ER46225.

APPENDIX A: THE 2DTSC AND 3DTI HAMILTONIANS

To study the emergence of topological surface superconductivity in $FeSe_{0.45}Te_{0.55}$, we consider a 3D system with N_z layers [see Fig. 1(a)]. The 2DTSC model previously introduced [17] to describe the emergence of topological surface superconductivity in $FeSe_{0.45}Te_{0.55}$, starts from the quasi-2D nature of superconductivity in $FeSe_{1-x}Te_x$, utilizing a five-band model that was shown to explain the emergence of a superconducting phase with $s_\pm$-wave symmetry in the α, β, and γ bands, which arise predominantly from the Fe d orbital [19–22]. These bands exhibit Fermi surfaces that are closed around the Γ and X/Y points in the 1Fe Brillouin zone. However, as we need to consider a 3D systems with N_z layers (in order to obtain Dirac cones on the 3DTI surfaces), the inclusion of the full five-band model is computationally prohibitive. We, therefore, consider a simplified version of the 2DTSC model [17] as given in Eq. (1), which nevertheless preserves the salient features of the full five-band model. In particular, it reproduces the experimentally observed [25] two Fermi surfaces that are closed around the Γ point, which are relevant for the coupling to the Dirac cone, as shown in Fig. 1(b).

Moreover, the magnetic nature of Fe suggests that the experimentally observed magnetism on the surface of $FeSe_{0.45}Te_{0.55}$ [3–5] arises from the Fe d orbitals, rather than the Te/Se orbitals, or the hybridized Te p_z and Fe d_{xz} orbitals that give rise to the 3DTI [2,11–13]. We, therefore, included the effect of the experimentally observed magnetization into the 2DTSC Hamiltonian as previously discussed [17]. As a result, not only superconductivity, but also a magnetization is proximity induced into the 3DTI. Finally, we note that rotational symmetry of the system requires that the magnetization and Rashba spin-orbit interaction possess opposite signs on the top and bottom surfaces, i.e., $J \to -J$ and $\alpha \to -\alpha$.

Moreover, for the calculations presented in the main text, we consider a 3DTI with a finite number of layers in the z direction, N_z. As a result, a Dirac cone appears on the top and bottom surfaces of the system. To demonstrate this, we present in Fig. 5(a) the electronic dispersion of the 3DTI only ($V = 0$) in the normal state, which exhibits the characteristic Dirac cone. A comparison of the (3DTI) c-electron spectral function on the surface layer [see Fig. 5(b)], and in the first layer below the surface [see Fig. 5(c)], demonstrates that the Dirac cone exists only on the surface of the 3DTI, and essentially possesses no spectral weight in the layers below the surface.

APPENDIX B: DERIVATION OF THE HYBRIDIZATION MATRICES BETWEEN THE 2DTSC AND THE 3DTI SYSTEMS

To derive the form of the hybridization elements, $V_{n,a,\sigma}$ [see Eq. (3)], we use that the coupled 2DTSC and 3DTI systems with a finite number of N_z layers in the z direction is invariant under rotation around the x axis. In the following, we first consider the symmetry properties of the 3DTI and 2DTSC separately, followed by a symmetry study of the coupled system.

1. Rotation symmetry of the 3DTI

The Hamiltonian of the 3DTI [26] in Eq. (2) can be written as $H_{3DTI} = \sum_{\mathbf{k}} \Psi^\dagger_{\mathbf{k}} \hat{\mathcal{H}}(\mathbf{k}, \lambda) \Psi_{\mathbf{k}}$ with spinor $\Psi^\dagger_{\mathbf{k}} = (c^\dagger_{\mathbf{k},1,\uparrow}, c^\dagger_{\mathbf{k},2,\uparrow}, c^\dagger_{\mathbf{k},1,\downarrow}, c^\dagger_{\mathbf{k},2,\downarrow})$ and

$$\hat{\mathcal{H}}(\mathbf{k}, \lambda) = \begin{pmatrix} -\mu_c + \xi_{\mathbf{k}} & i\lambda \sin(k_z) & 0 & \lambda[i \sin(k_x) + \sin(k_y)] \\ -i\lambda \sin(k_z) & -\mu_c - \xi_{\mathbf{k}} & \lambda[i \sin(k_x) + \sin(k_y)] & 0 \\ 0 & \lambda[-i \sin(k_x) + \sin(k_y)] & -\mu_c + \xi_{\mathbf{k}} & i\lambda \sin(k_z) \\ \lambda[-i \sin(k_x) + \sin(k_y)] & 0 & -i\lambda \sin(k_z) & -\mu_c - \xi_{\mathbf{k}} \end{pmatrix}, \quad \text{(B1)}$$

where $\xi_{\mathbf{k}} = m - 2t[\cos(k_x) + \cos(k_y) + \cos(k_z)]$. The Hamiltonian is invariant under a simultaneous rotation around the x axis, both in real and in spin space, and $\lambda \to -\lambda$, which is achieved using the unitary transformation,

$$\hat{M}_x = \sigma_x \otimes \sigma_z, \tag{B2}$$

with σ_i being the Pauli matrices, such that

$$\hat{M}_x \hat{\mathcal{H}}(k_x, -k_y, -k_z, \lambda)\hat{M}_x^\dagger = \hat{\mathcal{H}}(k_x, k_y, k_z, \lambda). \tag{B3}$$

For the system considered in the main text, the 3DTI consists of a finite number of N_z layers in the z direction. Moreover, as superconductivity is proximitized into the 3DTI, we need to write the Hamiltonian for the 3DTI with N_z layers in Nambu space, resulting in

$$\hat{\mathcal{H}}[k_x, k_y, i = (1, \ldots, N_z), \lambda] = \begin{pmatrix} \hat{\mathcal{H}}_1 & \hat{T}_z & 0 & 0 & 0 \\ \hat{T}_z^\dagger & \hat{\mathcal{H}}_2 & \hat{T}_z & 0 & 0 \\ 0 & \ddots & \ddots & \ddots & 0 \\ 0 & 0 & \hat{T}_z^\dagger & \hat{\mathcal{H}}_{N_z-1} & \hat{T}_z \\ 0 & 0 & 0 & \hat{T}_z^\dagger & \hat{\mathcal{H}}_{N_z} \end{pmatrix}, \tag{B4}$$

with spinor $\Psi_{\mathbf{k}}^\dagger = (\Psi_{1,\mathbf{k}}^\dagger, \Psi_{2,\mathbf{k}}^\dagger, \ldots, \Psi_{N_z,\mathbf{k}}^\dagger)$ where

$$\Psi_{i,\mathbf{k}}^\dagger = (c_{i,\mathbf{k},1,\uparrow}^\dagger, c_{i,\mathbf{k},2,\uparrow}^\dagger, c_{i,\mathbf{k},1,\downarrow}^\dagger, c_{i,\mathbf{k},2,\downarrow}^\dagger, c_{i,-\mathbf{k},1,\uparrow}, c_{i,-\mathbf{k},2,\uparrow}, c_{i,-\mathbf{k},1,\downarrow}, c_{i,-\mathbf{k},2,\downarrow}), \tag{B5}$$

and i being the layer index. Moreover, $\hat{\mathcal{H}}_i$ is the Hamiltonian in Nambu space of the i'th layer of the 3DTI given by

$$\hat{\mathcal{H}}_i(k_x, k_y) = \begin{pmatrix} \hat{\mathcal{H}}_i^n(k_x, k_y) & 0 \\ 0 & -[\hat{\mathcal{H}}_i^n(-k_x, -k_y)]^T \end{pmatrix}, \tag{B6}$$

where $\hat{\mathcal{H}}_i^n$ is the normal state Hamiltonian of the i'th layer of the 3DTI given by

$$\hat{\mathcal{H}}_i^n = \begin{pmatrix} -\mu_c + \varepsilon_{\mathbf{k}} & 0 & 0 & \lambda[i\,\sin(k_x) + \sin(k_y)] \\ 0 & -\mu_c - \varepsilon_{\mathbf{k}} & \lambda[i\,\sin(k_x) + \sin(k_y)] & 0 \\ 0 & \lambda[-i\,\sin(k_x) + \sin(k_y)] & -\mu_c + \varepsilon_{\mathbf{k}} & 0 \\ \lambda[-i\,\sin(k_x) + \sin(k_y)] & 0 & 0 & -\mu_c - \varepsilon_{\mathbf{k}} \end{pmatrix}, \tag{B7}$$

with $\varepsilon_{\mathbf{k}} = m - 2t[\cos(k_x) + \cos(k_y)]$. The hopping matrix $\hat{T}_z$ is given by

$$\hat{T}_z = \begin{pmatrix} \hat{t}_z & 0 \\ 0 & -\hat{t}_z^T \end{pmatrix}, \tag{B8}$$

where

$$\hat{t}_z = \begin{pmatrix} t & -\lambda & 0 & 0 \\ \lambda & -t & 0 & 0 \\ 0 & 0 & t & -\lambda \\ 0 & 0 & \lambda & -t \end{pmatrix}. \tag{B9}$$

Defining next

$$\hat{S}_x = \begin{pmatrix} 0 & 0 & \cdots & 0 & \hat{N}_x \\ 0 & \cdots & 0 & \hat{N}_x & 0 \\ \vdots & \vdots & \ddots & \vdots & \vdots \\ 0 & \hat{N}_x & 0 & \cdots & 0 \\ \hat{N}_x & 0 & \cdots & 0 & 0 \end{pmatrix}, \tag{B10}$$

where

$$\hat{N}_x = \begin{pmatrix} \hat{M}_x & 0 \\ 0 & \hat{M}_z \end{pmatrix}, \tag{B11}$$

the symmetry of Eq. (B3) becomes

$$\hat{S}_x^\dagger \hat{\mathcal{H}}[k_x, -k_y, i = (N_z, \ldots, 1), \lambda]\hat{S}_x = \hat{\mathcal{H}}[k_x, k_y, i = (1, \ldots, N_z), \lambda]. \tag{B12}$$

2. Rotation symmetry of the 2DTSC

The Hamiltonian for a single layer of the 2DTSC can be written as $H_{TSC} = \sum_{\mathbf{k}} \Phi_{\mathbf{k}}^{\dagger} \hat{H}_{TSC}(\mathbf{k}, \alpha, J) \Phi_{\mathbf{k}}$ with spinor $\Phi_{\mathbf{k}}^{\dagger} = (f_{\mathbf{k},\uparrow}^{\dagger}, f_{\mathbf{k},\downarrow}^{\dagger}, f_{-\mathbf{k},\uparrow}, f_{-\mathbf{k},\downarrow})$ and

$$\hat{H}_{TSC}(\mathbf{k}, \alpha, J) = \begin{pmatrix} \xi_{\mathbf{k}} + J & 2\alpha[i\,\sin(k_x) + \sin(k_y)] & 0 & \Delta \\ 2\alpha[-i\,\sin(k_x) + \sin(k_y)] & \xi_{\mathbf{k}} - J & -\Delta & 0 \\ 0 & -\Delta & -\xi_{\mathbf{k}} - J & 2\alpha[-i\,\sin(k_x) + \sin(k_y)] \\ \Delta & 0 & 2\alpha[i\,\sin(k_x) + \sin(k_y)] & -\xi_{\mathbf{k}} + J \end{pmatrix}, \tag{B13}$$

where $\epsilon_{\mathbf{k}} = -2t[\cos(k_x) + \cos(k_y)] - \mu$. Next, we define a unitary matrix $\hat{U}_x$ via

$$\hat{U}_x = \sigma_z \otimes \sigma_x = \begin{pmatrix} 0 & 1 & 0 & 0 \\ 1 & 0 & 0 & 0 \\ 0 & 0 & 0 & -1 \\ 0 & 0 & -1 & 0 \end{pmatrix}, \tag{B14}$$

which yields

$$\hat{U}_x^{\dagger} \hat{H}_{TSC}(k_x, -k_y, \Delta, -\alpha, -J) \hat{U}_x = \hat{H}_{TSC}(k_x, k_y, \Delta, \alpha, J). \tag{B15}$$

As we show in the next section, this symmetry operation is required, as a rotation of the entire coupled system around the x axis exchanges the top and bottom 2DTSC surfaces, which possess an opposite sign in the magnetization and Rashba spin-orbit interaction.

3. Rotation symmetry of the coupled 3DTI and 2DTSC systems

We next consider the rotation symmetry of the coupled 3DTI and 2DTSC systems. To this end, we consider a 3DTI with N_z layers, and only two layers of the 2DTSC system that are coupled to the top and bottom surfaces of the 3DTI system. As we discuss in the main text, and explicitly show in Appendix E, the bulk bands of the 2DTSC do not affect the electronic structure or topological phase on the surface of the system. Moreover, as the 2DTSC bulk layers do not contain a Rashba spin-orbit interaction or ferromagnetic magnetization, their rotation properties are trivial, and we will, therefore, omit them below for clarity of the derivation.

The Hamiltonian of the 3DTI with N_z layers and of the two 2DTSC layers is given by

$$\hat{H}_S(k_x, k_y, N_z, \alpha, J, \lambda) = \begin{pmatrix} \hat{H}_{TSC}(\alpha, J) & \hat{V}_t & 0 & 0 & 0 & 0 \\ \hat{V}_t^{\dagger} & \hat{\mathcal{H}}_1 & \hat{T}_z & 0 & 0 & 0 \\ 0 & \hat{T}_z^{\dagger} & \hat{\mathcal{H}}_2 & \hat{T}_z & 0 & 0 \\ 0 & 0 & \ddots & \ddots & \ddots & 0 \\ 0 & 0 & 0 & \hat{T}_z^{\dagger} & \hat{\mathcal{H}}_{N_z} & \hat{V}_b \\ 0 & 0 & 0 & 0 & \hat{V}_b^{\dagger} & \hat{H}_{TSC}(-\alpha, -J) \end{pmatrix}, \tag{B16}$$

with spinor $\Psi_{\mathbf{k}}^{\dagger} = (\Phi_{1,\mathbf{k}}^{\dagger}, \Psi_{1,\mathbf{k}}^{\dagger}, \Psi_{2,\mathbf{k}}^{\dagger}, \ldots, \Psi_{N_z,\mathbf{k}}^{\dagger}, \Phi_{N_z,\mathbf{k}}^{\dagger})$, and $\hat{V}_{t,b}$ are the hybridization matrices between the 2DTSC layers and the top and bottom 3DTI surface layers as described by Eq. (3). Using next

$$\hat{P} = \begin{pmatrix} 0 & 0 & 0 & 0 & 0 & \hat{U}_x \\ 0 & 0 & 0 & 0 & \hat{N}_x & 0 \\ 0 & 0 & 0 & \hat{N}_x & 0 & 0 \\ 0 & 0 & \cdots & 0 & 0 & 0 \\ 0 & \hat{N}_x & 0 & 0 & 0 & 0 \\ \hat{U}_x & 0 & 0 & 0 & 0 & 0 \end{pmatrix}, \tag{B17}$$

the invariance of the coupled system under rotation around the x axis yields

$$\hat{P}^{\dagger} \hat{H}_S(k_x, k_y, N_z, \alpha, J, \lambda) \hat{P} = \hat{H}_S(k_x, -k_y, N_z, \alpha, J, \lambda). \tag{B18}$$

This equation holds if

$$\begin{aligned} \hat{U}_x^{\dagger} \hat{V}_b \hat{N}_x &= \hat{V}_t^{\dagger}, \\ \hat{N}_x^{\dagger} \hat{V}_t \hat{U}_x &= \hat{V}_b^{\dagger}, \end{aligned} \tag{B19}$$

which is satisfied by choosing

$$\hat{V}_t = V\begin{pmatrix} 1 & -1 & 0 & 0 & 0 & 0 & 0 & 0 \\ 0 & 0 & 1 & -1 & 0 & 0 & 0 & 0 \\ 0 & 0 & 0 & 0 & -1 & 1 & 0 & 0 \\ 0 & 0 & 0 & 0 & 0 & 0 & -1 & 1 \end{pmatrix}, \quad V_b = V\begin{pmatrix} 1 & 0 & 0 & 0 \\ 1 & 0 & 0 & 0 \\ 0 & 1 & 0 & 0 \\ 0 & 1 & 0 & 0 \\ 0 & 0 & -1 & 0 \\ 0 & 0 & -1 & 0 \\ 0 & 0 & 0 & -1 \\ 0 & 0 & 0 & -1 \end{pmatrix}. \tag{B20}$$

For the results shown in the main text, we consider only coupled systems with an odd number of layers N_z. In this case, and to preserve the symmetry of the system, we take the hybridization matrices in layers $n = 1, \ldots, (N_z - 1)/2$ to be identical to $\hat{V}_t$, the hybridization matrices in layers $n = (N_z - 1)/2 + 2, \ldots, N_z$ to be identical to $\hat{V}_b$, and the hybridization matrix in layer $n = (N_z - 1)/2 + 1$ to be zero.

APPENDIX C: EVOLUTION OF SPECTRAL FUNCTIONS BELOW T_c

In Figs. 2(a)–2(c), we presented the evolution of the electronic dispersion and of the (3DTI) c-electron spectral function with increasing JS below T_c. In Fig. 6, we reproduce the results of Figs. 2(a)–2(c), together with the spectral function of the (2DTSC) f electrons. It is interesting to note that neither the spectral function of the c electrons, nor that of the f electrons possesses any considerable weight in the negative energy branch of the band in which the gap closing occurs (see Fig. 6). Thus, independent of whether ARPES experiments probe the c- or f-electron orbitals [28], the gap closing will be difficult to observe.

APPENDIX D: GAP CLOSINGS IN THE (V, JS)-PLANE

As mentioned in the main text, a gap closing in the (V, JS) plane occurs only at the Γ point. Here, we demonstrate that there are no additional gap closings that occur at any other momenta in the Brillouin zone. To this end, we define the gap $E_{\min}$ as the minimum positive energy for any momentum in the Brillouin zone, i.e., $E_{\min} = \min_{\mathbf{k}\in BZ}(|E_{\mathbf{k}}|)$. Since determining

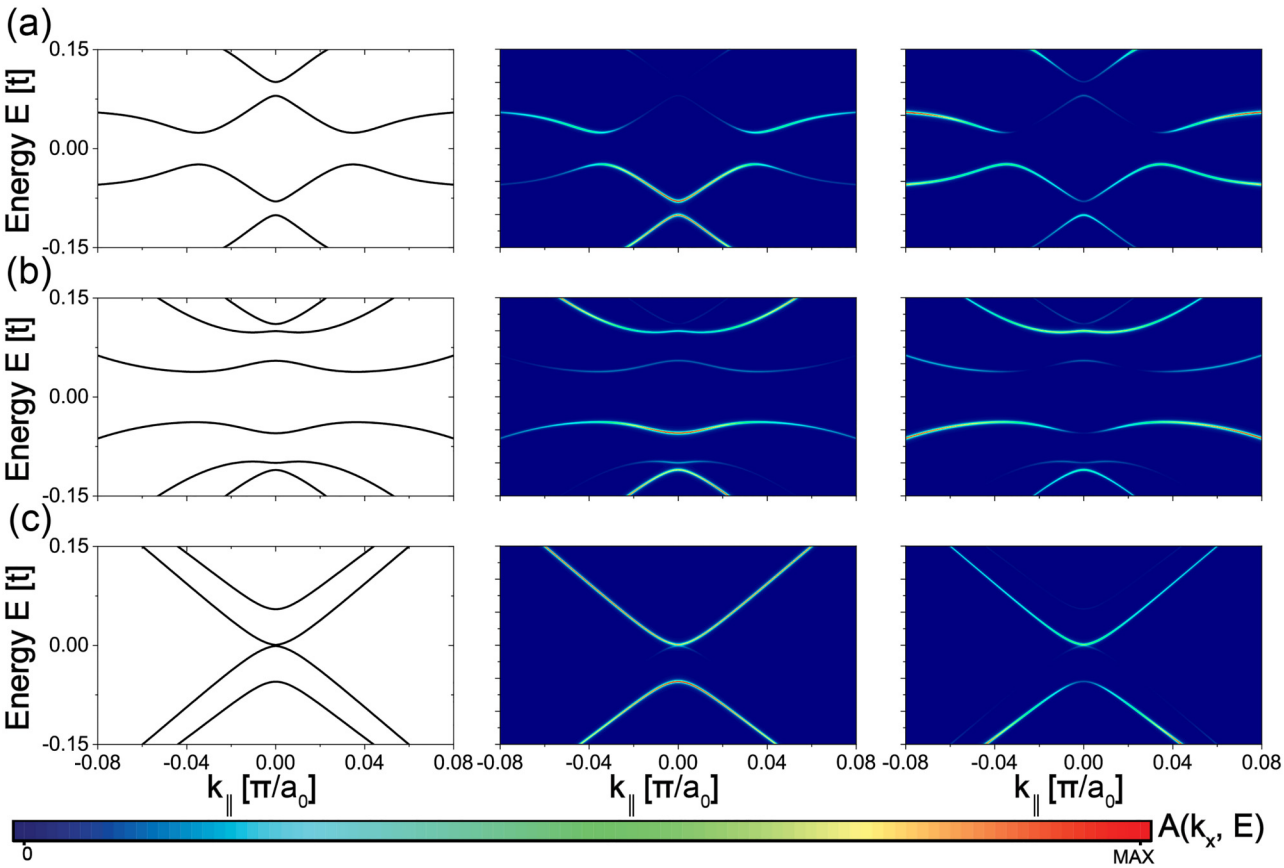

FIG. 6. Evolution of the electronic dispersion (left column), (3DTI) c-electron (middle column) and (2DTSC) f-electron spectral functions (right column) below T_c with increasing JS as a function of k_x for $k_y = 0$: (a) $(JS, \mu_c) = (0.1, 0.06)t$, (b) $(JS, \mu_c) = (0.2, 0.04)t$, and (c) $(JS, \mu_c) = (0.45, 0.04)t$. Parameters are $(V, \Delta_0, \alpha, \mu) = (0.07, 0.1, 0.1, 3.8)t$.

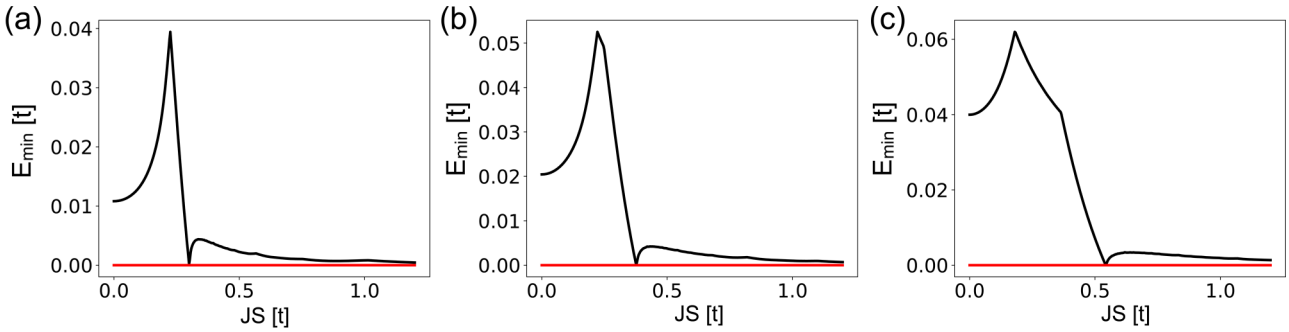

FIG. 7. $E_{\min}$ of the coupled 3DTI and 2DTSC systems as a function of JS for (a) $V = 0.05t$, (b) $V = 0.07t$, and (c) and $V = 0.1t$.

$E_{\min}$ for an extended range of parameters on the (V, JS) plane is computationally very demanding, we consider only line cuts of $E_{\min}$ as function of JS for several values of the hybridization strength V as shown in Fig. 7. For all line cuts we considered, only a single gap closing occurs, which coincides with the gap closing at the Γ point shown in Fig. 2(d). Thus, we conclude that for the coupled 2DTSC and 3DTI systems, gap closings, which indicate a topological phase transition, occur only at the Γ point.

APPENDIX E: RELEVANCE OF BULK 2DTSC LAYERS

We argued in the main text that the bulk 2DTSC layers that couple to the bulk 3DTI layers do not affect the surface electronic structure or the topological surface phase. The reason for this is twofold. First, the 2DTSC system itself exhibits a (quasi-)2D structure with no direct coupling between the 2DTSC layers. This implies that the bulk 2DTSC layers cannot directly couple to the 2DTSC or 3DTI surface layers, only indirectly by hybridizing with the bulk 3DTI layers. This hybridization, however, is strongly suppressed since, second, the bulk 3DTI layers possesses a gap of $E_g = t$. Thus, the bulk 3DTI layers cannot hybridize with the low-energy states of the bulk 2DTSC layers. Here, we demonstrate this explicitly by computing the electronic structure on the surface with and without the 2DTSC bulk bands, retaining in both cases the two 2DTSC layers that couple to the top and bottom surface layers of the 3DTI. In Fig. 8, we present the resulting surface electronic structure for several values of JS when surface and bulk 2DTSC layers are included (black solid line), and when only the two surface 2DTSC layers are included (red dashed line). These two results are essentially indistinguishable, implying that the bulk 2DTSC layers have no effects on the low-energy electronic structure of the surface. Moreover, we find that the absence of the bulk 2DTSC layers does also not alter the gap map shown in Fig. 2(d), implying that the bulk 2DTSC layers do not affect the topological surface state of the hybridized system. To reduce the computationally complexity of our calculations, and to ensure that we can consider sufficiently large system sizes, we, therefore, neglect the bulk 2DTSC layers when studying the electronic structure in vortex cores and along domain walls.

APPENDIX F: MZM IN A VORTEX CORE

For the calculation of the electronic structure around a vortex core, we consider a system that is finite in the x, y, and z directions with the system's length in these directions given by $l_i = N_i a_0$ $(i = x, y, z)$ with a_0 being the lattice constant. For the results shown in Fig. 3, we use two parameter sets characteristic of regions I and II. For region I [see Figs. 3(a) and 3(c)], we present the c-electron LDOS (summed over both orbitals) for parameters $(JS, \Delta_0, \mu_c, V, \alpha, \mu) = (0.0, 0.1, 0.06, 0.07, 0.1, 3.8)t$ and system size $(N_x, N_y, N_z) = (81, 81, 7)$. For region II, we present [see Figs. 3(b) and 3(d)] the f-electron LDOS with parameters $(JS, \Delta_0, \mu_c, V, \alpha, \mu) = (0.9, 0.6, 0.04, 0.07, 0.1, 3.8)t$ and system size $(N_x, N_y, N_z) = (151, 151, 3)$. To simulate a magnetic vortex core in such a system, one typically introduces the magnetic field via a Peierls' substitution [17],

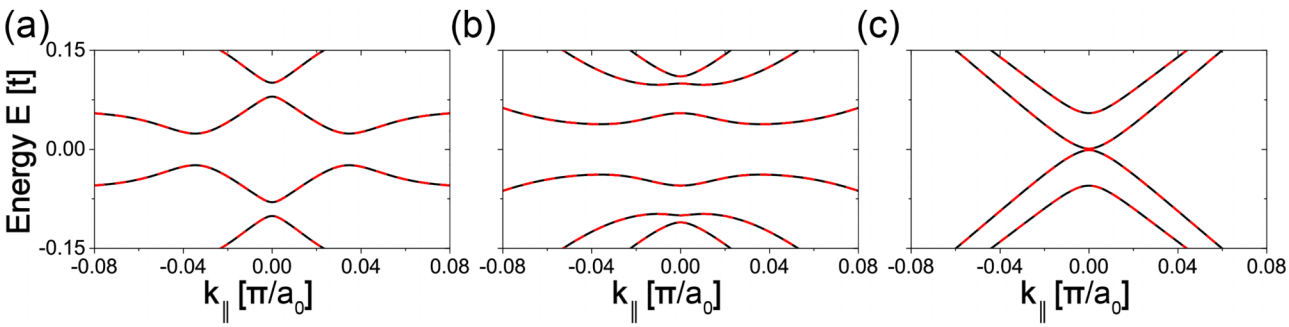

FIG. 8. Evolution of the electronic dispersion below T_c with increasing JS as a function of k_x for $k_y = 0$: (a) $(JS, \mu_c) = (0.1, 0.06)t$, (b) $(JS, \mu_c) = (0.2, 0.04)t$, and (c) $(JS, \mu_c) = (0.45, 0.04)t$. Black solid (red dashed) line represents the electronic structure when all surface and bulk 2DTSC layers (when only the surface 2DTSC layers) are included. Parameters are $(V, \Delta_0, \alpha, \mu) = (0.07, 0.1, 0.1, 3.8)t$ and $N_z = 5$.

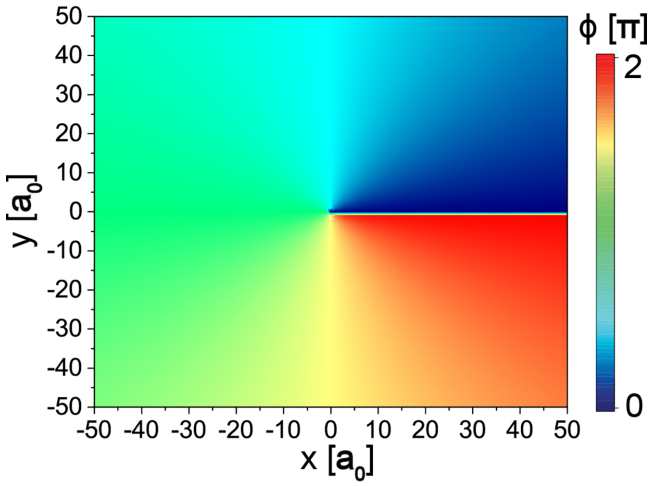

FIG. 9. Phase angle $\phi(\mathbf{r})$ as a function of position for the calculations shown in Fig. 3.

and computes the superconducting order parameter self-consistently. This approach, however, is computationally very demanding for the coupled 2DTSC and 3DTI systems, and the required system sizes. We, therefore, employ a simpler approach, which has previously been used to study the emergence of MZMs in vortex cores [16]. In this approach, one simulates a vortex core by imposing a phase winding of the superconducting order parameter $\Delta(\mathbf{r}) = \Delta_0 e^{i\phi(\mathbf{r})}$ around the vortex core. The spatial dependence of the phase $\phi(\mathbf{r})$ is shown in Fig. 9. As the magnetic flux penetrates the system from the bottom to the top surface, we assign the same superconducting phases on both surfaces. The LDOS in the vicinity of a vortex core for parameters characteristic for regions I and II are shown in Fig. 3.

We note that the small energy splitting of the MZMs shown in Fig. 3 is the result of the finite size of the system, and the resulting hybridization between MZMs. Specifically, in region I, where the topological phase arises from the 3DTI mechanism, the energy splitting between the MZMs decreases with increasing number of layers N_z, i.e., with increasing separation between the two MZMs on the top and bottom surfaces. In contrast, in region II, the energy splitting decreases with increasing N_x, N_y as the 2DTSC exhibits MZMs not only in a vortex core, but also at the edge of the system as was previously discussed [29]. A comparison of the LDOS as a function of energy and distance from the vortex core in region II on the top surface [see Fig. 10(a)], and on the first layer below the surface [see Fig. 10(b)], using the same intensity scale, shows that the MZM as well as the trivial CdGM states are entirely confined to the surface layer. This is expected for the MZM as only the surface layer is topological. However, since the CdGM states shown Fig. 10(a) are associated with the superconducting gap that is opened in the Dirac cone (the latter existing only on the surface, see Fig. 5), they are also necessarily confined to the surface.

APPENDIX G: MAJORANA EDGE MODES AT DOMAIN WALLS

In Fig. 4, we computed the electronic dispersion near a PPDW and SDW in regions I and II using the parameters $(V, \alpha, \mu) = (0.07, 0.1, 3.8)t$. For region I, we used a characteristic parameter set given by $(JS, \Delta_0, \mu_c) = (0.1, 0.1, 0.06)t$, whereas for region II, we used $(JS, \Delta_0, \mu_c) = (0.9, 0.6, 0.04)t$. The system is implemented using periodic boundary conditions such that it possesses two domain walls. The spectral functions are shown to the right of the domain walls, which are located between two columns of sites. We computed the electronic structure for the PPDW in region I (region II) using a scattering potential of $U_0 = 0.1$t. ($U_0 = 0.5t$) [see Eq. (G1)].

Moreover, since the systems exhibits two domain walls, we can investigate the helical or chiral nature of the Majorana edge modes by considering the spin-resolved spectral functions at both domain walls. In Fig. 11(a) we present the the electronic dispersion shown in Fig. 4 for the PPDW in region I, and in Figs. 11(b)–11(e) the spin-resolved (3DTI) c-electron spectral functions at both domain walls. Although the spectral functions exhibit a significant spin dependence, they are identical at both domain walls, implying that the Majorana edge mode at a PPDW is neither helical nor chiral. In contrast, a comparison of the electronic dispersion for a SDW in region II, shown in Fig. 11(f), and the corresponding spin-resolved (2DTSC) f-electron spectral functions shown in Figs. 11(g)–11(j), clearly reveal the chiral nature of the Majorana edge mode.

Moreover, Majorana edge modes are topologically protected and, thus, robust against disorder effects. To demonstrate this robustness, we study the effects of disorder on the Majorana edge modes at a PPDW in region I [see Fig. 4(a)], and at a SDW in region II [see Fig. 4(c)]. To this end, we introduce a nonmagnetic scattering potential along the domain

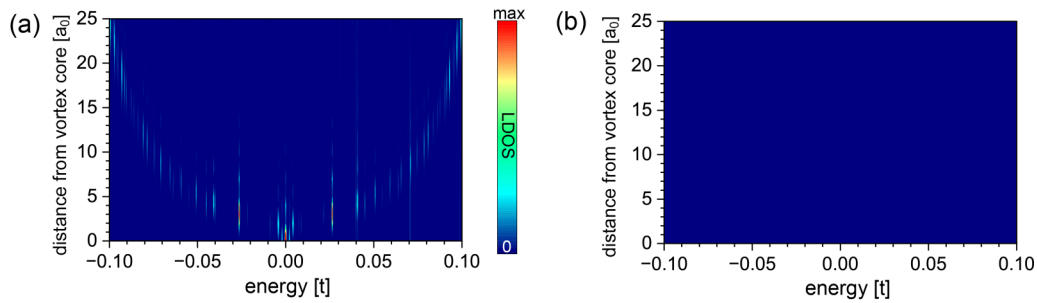

FIG. 10. LDOS as a function of energy and distance from the vortex core in region II (a) on the top surface, and (b) on the first layer below the surface. Parameters are $(JS, \Delta_0, \mu_c, V, \alpha, \mu) = (0.9, 0.6, 0.04, 0.07, 0.1, 3.8)t$, and system size $(N_x, N_y, N_z) = (71, 71, 5)$.

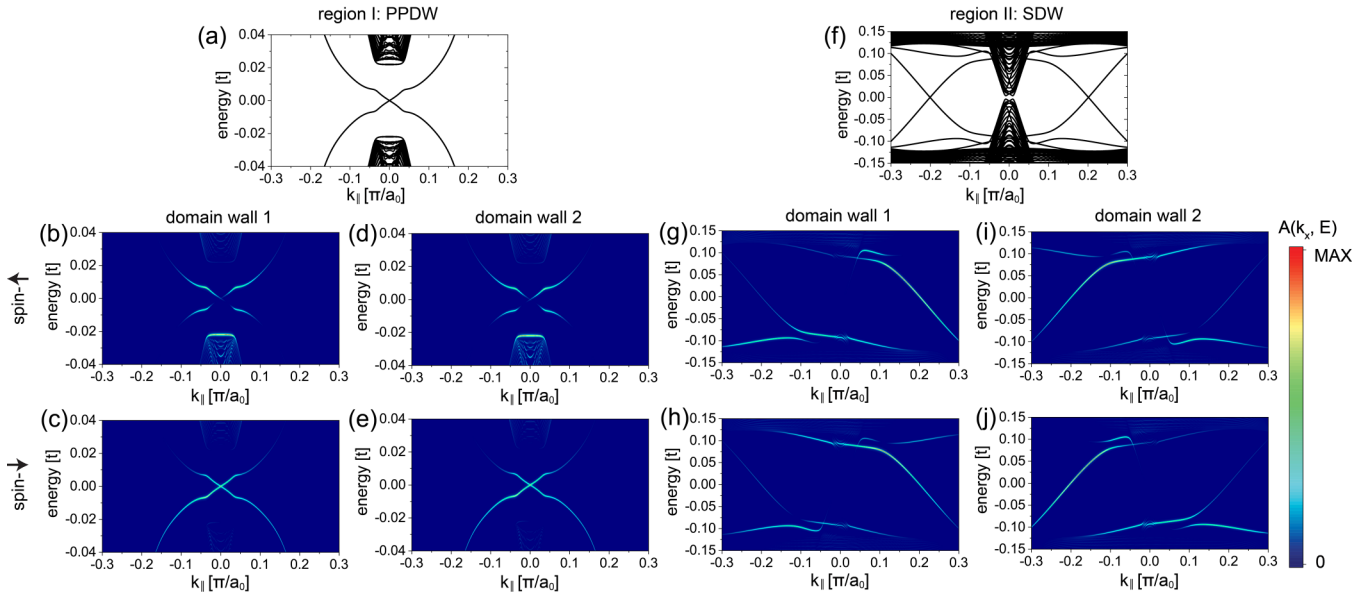

FIG. 11. (a) Electronic dispersion as a function of momentum along a PPDW in region I. (b)–(e) Corresponding spin-resolved (3DTI) c-electron spectral functions to the right of domain-wall 1 (left column) and domain-wall 2 (right column). The spectral functions are summed over both c-electron orbitals, and parameters are $(V, \alpha, \mu, JS, \Delta_0, \mu_c, U_0) = (0.07, 0.1, 3.8, 0.1, 0.1, 0.06, 0.1)t$. (f) Electronic dispersion as a function of momentum along a SDW in region II. (g)–(j) Corresponding spin-resolved (2DTSC) f-electron spectral functions to the right side of domain-wall 1 (left column) and domain-wall 2 (right column). Parameters are $(V, \alpha, \mu, JS, \Delta_0, \mu_c, U_0) = (0.07, 0.1, 3.8, 0.9, 0.6, 0.04, 0.0)t$ and $N_z = 5$.

wall on the two surfaces, defined via

$$\hat{H}_{\text{scat}} = U_0 \sum_{n=1,N_z} \sum_{\mathbf{R}} \sum_{\mathbf{k}_\parallel} \times \left(f^\dagger_{n,\mathbf{k}_\parallel,\mathbf{R},\sigma} f_{n,\mathbf{k}_\parallel,\mathbf{R},\sigma} + \sum_{a=1,2} c^\dagger_{n,\mathbf{k}_\parallel,\mathbf{R},a,\sigma} c_{n,\mathbf{k}_\parallel,\mathbf{R},a,\sigma} \right), \tag{G1}$$

where U_0 is the scattering strength, n is the layer index, $\mathbf{R}$ denotes sites next to the domain wall (which is located between two lattice points), and $\mathbf{k}_\parallel$ is the momentum parallel to the domain wall. In Fig. 12, we present the electronic dispersion for a PPDW in region I and a SDW in region II for different values of U_0. Note that the existence of Majorana edge modes as well as the number of these modes are unaffected by the scattering potential as expected for topologically protected Majorana edge modes.

Finally, we considered the effects of a finite width of the spin-domain wall on its electronic structure in region II. To this end, we assume that the spin rotates gradually in the plane perpendicular to the direction of the domain wall by an angle of $\theta = \pi/N_w$ between neighboring sites, where N_w is the width of the domain wall. In Figs. 13(a) and 13(b), we present the electronic dispersion as a function of the momentum parallel to the domain wall for a domain wall of width $N_w = a_0$ [see Fig. 13(a)], corresponding to the domain wall discussed in Fig. 4 and of width $N_w = 10a_0$. In agreement with the bulk-boundary correspondence, we find that the finite width of the domain wall does not affect the existence of the chiral Majorana edge modes. A line cut of the (normalized) zero-energy LDOS perpendicular to the domain wall, as shown in Fig. 13(c), demonstrates that for both cases, $N_w = a_0$ and $N_w = 10a_0$, the Majorana modes is localized at the domain wall, although the localization length increases with increasing domain-wall width. We, thus, conclude, that a finite width of the spin domain wall does not have any

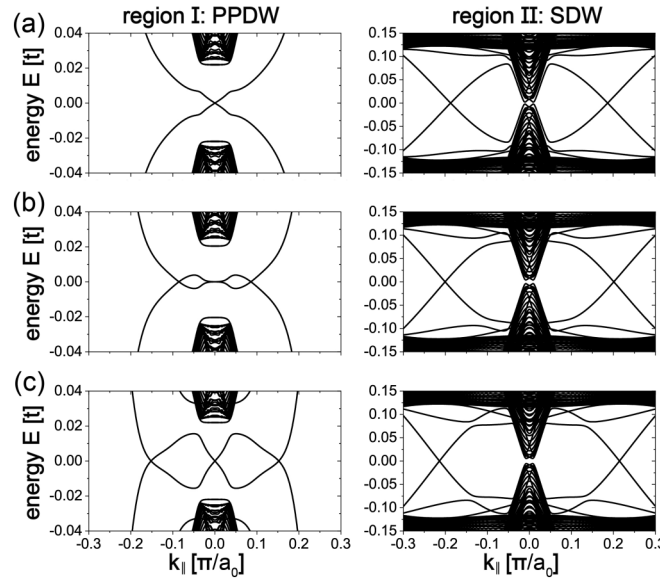

FIG. 12. Electronic dispersion at domain walls in the presence of a nonmagnetic scattering potential for a PPDW in region I (left column) and a SDW in region II (right column). (a) Electronic dispersions for a scattering potential of $U_0 = 0.1t$. (b) Electronic dispersions for zero scattering potential. (c) Electronic dispersions for $U_0 = -0.1t$. Parameters in region I are $(V, \alpha, \mu, JS, \Delta_0, \mu_c) = (0.07, 0.1, 3.8, 0.1, 0.1, 0.06)t$, whereas, in region II, we employed $(V, \alpha, \mu, JS, \Delta_0, \mu_c) = (0.07, 0.1, 3.8, 0.9, 0.6, 0.04)t$.

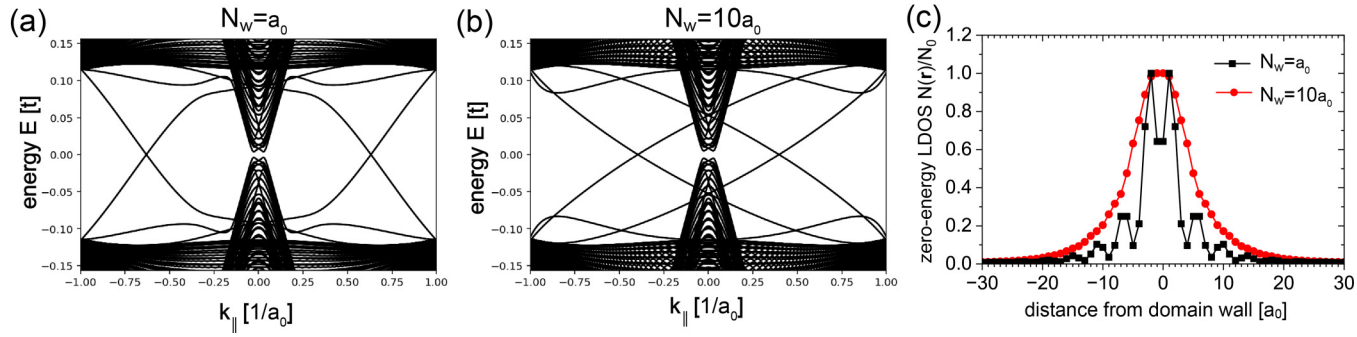

FIG. 13. Electronic dispersion as a function of momentum along the domain wall for spin-domain walls of width (a) $N_w = a_0$, and (b) $N_w = 10a_0$ in region II. In both cases, a chiral Majorana edge mode exists at the domain wall, in agreement with the results shown in Fig. 4. (c) Line cut of the zero-energy LDOS perpendicular to the domain wall for $N_w = a_0$ and $N_w = 10a_0$. To facilitate a comparison of the results, we have normalized the LDOS by its largest value along the line cut. Parameters are $(V, \alpha, \mu, JS, \Delta_0, \mu_c) = (0.07, 0.1, 3.8, 0.9, 0.6, 0.04)t$.

qualitative effect on the existence of a chiral Majorana edge mode or the localization of the mode. The results presented in Fig. 4, thus, also hold for a finite width of the domain walls.

APPENDIX H: PERSISTENT SUPERCURRENTS ALONG DOMAIN WALLS

The supercurrents flowing parallel to the domain wall possess two contributions, one each from a current flowing between the 2DTSC f orbitals and the 3DTI c orbitals. There is no current flowing between the 2DTSC and the 3DTI orbitals parallel to the domain wall as the hybridization is local, i.e., on site.

The persistent supercurrent associated with the hopping of an electron from a site $\mathbf{r}$ to a nearest-neighbor site $\mathbf{r}+\boldsymbol{\delta}$ between 3DTI orbitals is given by

$$I^{3DTI}_{\mathbf{r},\mathbf{r}+\boldsymbol{\delta}} = -\frac{2e}{\hbar}\sum_{\sigma,\sigma'}\sum_{a,b=1,2}\int\frac{d\omega}{2\pi}\mathrm{Re}\{[-t_{aa}\delta_{ab}\delta_{\sigma\sigma'} + i\lambda(\boldsymbol{\delta}\times\boldsymbol{\sigma})^z_{\sigma\sigma'}\delta_{a\bar{b}}]g^<_{b,\sigma';a,\sigma}(\mathbf{r}+\boldsymbol{\delta},\mathbf{r},\omega)\}, \quad \text{(H1)}$$

where $-t_{aa}$ is the intraorbital hopping amplitude between nearest-neighbor sites, and λ is the Rashba spin-orbit interaction in the 3DTI system, see Eq. (2). The persistent current between the 2DTSC orbitals is given by

$$I^{2DTSC}_{\mathbf{r},\mathbf{r}+\boldsymbol{\delta}} = -\frac{2e}{\hbar}\sum_{\sigma,\sigma'}\int\frac{d\omega}{2\pi}\mathrm{Re}\{[-t\delta_{\sigma\sigma'} + i\alpha(\boldsymbol{\delta}\times\boldsymbol{\sigma})^z_{\sigma\sigma'}] \times g^<_{\sigma';\sigma}(\mathbf{r}+\boldsymbol{\delta},\mathbf{r},\omega)\}, \quad \text{(H2)}$$

where $-t$ is the hopping amplitude between nearest-neighbor sites, and α is the Rashba spin-orbit interaction in the 2DTSC system, see Eq. (1). Moreover, $g^<_{a,\sigma;b,\sigma'}(\mathbf{r},\mathbf{r}+\boldsymbol{\delta},\omega)$ $[g^<_{\sigma;\sigma'}(\mathbf{r},\mathbf{r}+\boldsymbol{\delta},\omega)]$ are the $(a,\sigma;b,\sigma')$ $[(\sigma;\sigma')]$ elements in Nambu space of the lesser Green's function matrices in the 3DTI [2DTSC] system. To compute the lesser Green's functions, we rewrite the Hamiltonian of Eq. (B16) for a ribbon geometry. Diagonalizing this Hamiltonian then allows us to compute the lesser Green's functions from the resulting eigenvectors and eigenvalues [17].

[1] C. Nayak, S. H. Simon, A. Stern, M. Freedman, and S. Das Sarma, Non-Abelian anyons and topological quantum computation, Rev. Mod. Phys. **80**, 1083 (2008).

[2] P. Zhang, K. Yaji, T. Hashimoto, Y. Ota, T. Kondo, K. Okazaki, Z. Wang, J. Wen, G. D. Gu, H. Ding, and S. Shin, Observation of topological superconductivity on the surface of an iron-based superconductor, Science **360**, 182 (2018).

[3] J. D. Rameau, N. Zaki, G. D. Gu, P. D. Johnson, and M. Weinert, Interplay of paramagnetism and topology in the Fe-chalcogenide high-T_c superconductors, Phys. Rev. B **99**, 205117 (2019).

[4] N. Zaki, G. Gu, A. Tsvelik, C. Wu, and P. D. Johnson, Time-reversal symmetry breaking in the Fe-chalcogenide superconductors, Proc. Natl. Acad. Sci. USA **118**, e2007241118 (2021).

[5] Y. Li, N. Zaki, V. O. Garlea, A. T. Savici, D. Fobes, Z. Xu, F. Camino, C. Petrovic, G. Gu, P. D. Johnson, J. M. Tranquada, and I. A. Zaliznyak, Electronic properties of the bulk and surface states of $Fe_{1+y}Te_{1-x}Se_x$, Nat Mater. **20**, 1221 (2021).

[6] D. Wang, L. Kong, P. Fan, H. Chen, S. Zhu, W. Liu, L. Cao, Y. Sun, S. Du, J. Schneeloch, R. Zhong, G. Gu, L. Fu, H. Ding, and H.-J. Gao, Evidence for Majorana bound states in an iron-based superconductor, Science **362**, 333 (2018).

[7] T. Machida, Y. Sun, S. Pyon, S. Takeda, Y. Kohsaka, T. Hanaguri, T. Sasagawa, and T. Tamegai, Zero-energy vortex bound state in the superconducting topological surface state of Fe(Se,Te), Nat. Mater. **18**, 811 (2019).

[8] L. Kong, S. Zhu, M. Papaj, H. Chen, L. Cao, H. Isobe, Y. Xing, W. Liu, D. Wang, P. Fan, Y. Sun, S. Du, J. Schneeloch, R. Zhong, G. Gu, L. Fu, H.-J. Gao, and H. Ding, Half-integer level shift of vortex bound states in an iron-based superconductor, Nat. Phys. **15**, 1181 (2019).

[9] S. Zhu, L. Kong, L. Cao, H. Chen, M. Papaj, S. Du, Y. Xing, W. Liu, D. Wang, C. Shen, F. Yang, J. Schneeloch, R. Zhong, G. Gu, L. Fu, Y.-Y. Zhang, H. Ding, and H.-J. Gao, Nearly quantized conductance plateau of vortex zero mode in an iron-based superconductor, Science **367**, 189 (2020).

[10] Z. Wang, J. O. Rodriguez, L. Jiao, S. Howard, M. Graham, G. D. Gu, T. L. Hughes, D. K. Morr, and V. Madhavan, Evidence for dispersing 1D Majorana channels in an iron-based superconductor, Science **367**, 104 (2020).

[11] Z. Wang, P. Zhang, G. Xu, L. K. Zeng, H. Miao, X. Xu, T. Qian, H. Weng, P. Richard, A. V. Fedorov, H. Ding, X. Dai, and Z. Fang, Topological nature of the $FeSe_{0.5}Te_{0.5}$ superconductor, Phys. Rev. B **92**, 115119 (2015).

[12] X. Wu, S. Qin, Y. Liang, H. Fan, and J. Hu, Topological characters in $Fe(Te_{1-x}se_x)$ thin films, Phys. Rev. B **93**, 115129 (2016).

[13] G. Xu, B. Lian, P. Tang, X.-L. Qi, and S.-C. Zhang, Topological Superconductivity on the Surface of Fe-Based Superconductors, Phys. Rev. Lett. **117**, 047001 (2016).

[14] L. Fu and C. L. Kane, Superconducting Proximity Effect and Majorana Fermions at the Surface of a Topological Insulator, Phys. Rev. Lett. **100**, 096407 (2008).

[15] N. J. McLaughlin, H. Wang, M. Huang, E. Lee-Wong, L. Hu, H. Lu, G. Q. Yan, G. Gu, C. Wu, Y.-Z. You, and C. R. Du, Strong correlation between superconductivity and ferromagnetism in an fe-chalcogenide superconductor, Nano Lett. **21**, 7277 (2021).

[16] X. Wu, S. B. Chung, C. Liu, and E.-A. Kim, Topological orders competing for the Dirac surface state in FeSeTe surfaces, Phys. Rev. Res. **3**, 013066 (2021).

[17] E. Mascot, S. Cocklin, M. Graham, M. Mashkoori, S. Rachel, and D. K. Morr, Topological surface superconductivity in $FeSe_{0.45}Te_{0.55}$, Commun. Phys. **5**, 188 (2022).

[18] K. H. Wong, E. Mascot, V. Madhavan, D. J. Van Harlingen, and D. K. Morr, Shot noise and differential conductance as signatures of putative topological superconductivity in $FeSe_{0.45}Te_{0.55}$, Phys. Rev. B **105**, L220504 (2022).

[19] H. Eschrig and K. Koepernik, Tight-binding models for the iron-based superconductors, Phys. Rev. B **80**, 104503 (2009).

[20] M. D. Watson, T. K. Kim, A. A. Haghighirad, N. R. Davies, A. McCollam, A. Narayanan, S. F. Blake, Y. L. Chen, S. Ghannadzadeh, A. J. Schofield, M. Hoesch, C. Meingast, T. Wolf, and A. I. Coldea, Emergence of the nematic electronic state in FeSe, Phys. Rev. B **91**, 155106 (2015).

[21] M. D. Watson, T. K. Kim, L. C. Rhodes, M. Eschrig, M. Hoesch, A. A. Haghighirad, and A. I. Coldea, Evidence for unidirectional nematic bond ordering in FeSe, Phys. Rev. B **94**, 201107(R) (2016).

[22] A. Kreisel, P. Hirschfeld, and B. Andersen, On the remarkable superconductivity of FeSe and its close cousins, Symmetry **12**, 1402 (2020).

[23] S. Graser, T. A. Maier, P. J. Hirschfeld, and D. J. Scalapino, Near-degeneracy of several pairing channels in multiorbital models for the Fe pnictides, New J. Phys. **11**, 025016 (2009).

[24] S. Sarkar, J. Van Dyke, P. O. Sprau, F. Massee, U. Welp, W.-K. Kwok, J. C. S. Davis, and D. K. Morr, Orbital superconductivity, defects, and pinned nematic fluctuations in the doped iron chalcogenide $FeSe_{0.45}Te_{0.55}$, Phys. Rev. B **96**, 060504(R) (2017).

[25] S. V. Borisenko, D. V. Evtushinsky, Z.-H. Liu, I. Morozov, R. Kappenberger, S. Wurmehl, B. Buechner, A. N. Yaresko, T. K. Kim, M. Hoesch, T. Wolf, and N. D. Zhigadlo, Direct observation of spin-orbit coupling in iron-based superconductors, Nat. Phys. **12**, 311 (2016).

[26] G. Schubert, H. Fehske, L. Fritz, and M. Vojta, Fate of topological-insulator surface states under strong disorder, Phys. Rev. B **85**, 201105(R) (2012).

[27] D. Crawford, E. Mascot, D. K. Morr, and S. Rachel, High-temperature Majorana fermions in magnet-superconductor hybrid systems, Phys. Rev. B **101**, 174510 (2020).

[28] J. A. Sobota, Y. He, and Z.-X. Shen, Angle-resolved photoemission studies of quantum materials, Rev. Mod. Phys. **93**, 025006 (2021).

[29] S. Rachel, E. Mascot, S. Cocklin, M. Vojta, and D. K. Morr, Quantized charge transport in chiral Majorana edge modes, Phys. Rev. B **96**, 205131 (2017).

[30] J. E. Hoffman, K. McElroy, D.-H. Lee, K. M. Lang, H. Eisaki, S. Uchida, and J. C. Davis, Imaging quasiparticle interference in $Bi_2Sr_2CaCu_2O_{8+\delta}$, Science **297**, 1148 (2002).

[31] C. Xu and D. K. Morr, Quasi-particle interference and majorana edge modes in topological superconductors, in preparation (2023).

[32] E. M. Spanton, K. C. Nowack, L. Du, G. Sullivan, R.-R. Du, and K. A. Moler, Images of Edge Current in InAs/GaSb Quantum Wells, Phys. Rev. Lett. **113**, 026804 (2014).